J Mater Sci (2012) 47:176–183
DOI 10.1007/s10853-011-5785-0

Synthesis of highly stable magnesium fluoride suspensions and their application in the corrosion protection of a Magnesium alloy

Florian Waltz · Mark A. Swider · Petra Hoyer · Thomas Hassel · Martin Erne · Kai Möhwald · Matthias Adlung · Armin Feldhoff · Claudia Wickleder · Friedrich-Wilhelm Bach · Peter Behrens

Received: 18 April 2011 / Accepted: 11 July 2011 / Published online: 28 July 2011

Abstract This study presents a new approach to enhance the corrosion resistance of tungsten inert gas (TIG) welded AZ31 magnesium alloys by using nanocrystalline magnesium fluoride suspensions in a suspension plasma spray (SPS) process. We have developed a synthesis for the preparation of nanocrystalline magnesium fluoride suspensions, which delivers nearly monodisperse nanoparticles in a gram scale yield. The particles were analyzed with transmission electron microscopy (TEM) and powder X-ray diffraction (PXRD). Stable suspensions of magnesium fluoride nanoparticles in water were characterized by dynamic light scattering (DLS), zeta-potential, and viscosity measurements. Such suspensions were deposited with an SPS torch onto TIG welded seams of the magnesium alloy AZ31, thus producing a protective magnesium fluoride layer. Magnesium fluoride covered welded seams were investigated by scanning electron microscopy (SEM), X-ray diffraction (XRD), and energy dispersive X-ray spectroscopy (EDXS). In order to introduce a simple method for sensoring the deposited magnesium fluoride coatings, the magnesium fluoride nanoparticles can also be fluorescence-labeled by co-doping with cerium(III) and terbium(III), the respective optical properties were characterized by reflection and luminescence spectroscopy. The deposited layers can, thus, be inspected by illumination with an UV lamp, because of their bright green emission. The corrosion properties of the magnesium fluoride layer on the welded seams were studied by means of potentiodynamic potential measurements.

F. Waltz · P. Behrens
Institut für Anorganische Chemie, Leibniz Universität Hannover, Callinstr. 9, 30167 Hannover, Germany

F. Waltz · A. Feldhoff · P. Behrens (✉)
ZFM—Center for Solid-State Chemistry and New Materials, Leibniz Universität Hannover, Hannover, Germany
e-mail: peter.behrens@acb.uni-hannover.de

M. A. Swider · P. Hoyer · T. Hassel · M. Erne · K. Möhwald · Fr.-W. Bach
Institut für Werkstoffkunde, Leibniz Universität Hannover, An der Universität 2, 30823 Garbsen, Germany

M. Adlung · C. Wickleder
Anorganische Chemie, Department Chemie und Biologie, Universität Siegen, Adolf-Reichwein-Straße, 57068 Siegen, Germany

A. Feldhoff
Institut für Physikalische Chemie und Elektrochemie, Leibniz Universität Hannover, Callinstr. 3A, 30167 Hannover, Germany

Introduction

For lightweight applications in automobiles, aircrafts as well as everyday items like cell phones, laptops, etc., magnesium alloys have become a major structural material [1, 2]. The increasing number of the use of magnesium alloys is caused by the superior strength-to-weight ratio when compared to commonly used metals such as aluminum and iron. Besides the advantages of reduction of weight and also good recyclability, the corrosion problems posed by magnesium alloys cannot be neglected [1]. Thus, a widespread use of magnesium alloys is still limited [3, 4]. The best protection against corrosion shows high purity magnesium, but the magnesium alloy AZ31, for example, has gained widespread acceptance in automotive applications due to a better balance between mechanical properties and corrosion protection. In aqueous environments magnesium instantaneously forms a magnesium hydroxide layer, which serves as a good protection at elevated pH

values (a pH value of 11 is observed due to the equilibrium solubility of $Mg(OH)_2$). This film protects the magnesium against corrosion as long as the local pH does not decrease below 11 and as long as no complexing ("damaging) species such as chloride, sulphate, or nitrate are present [3, 4]. However, small amounts of impurities in the magnesium alloy such as Ni, Fe, Cu, Zn, or Al multi-phase systems lead to the formation of galvanic cells which can initiate the corrosion by microgalvanic attack [5, 6]. In fact, for a widespread industrial use, AZ31 has to be protected by passive surface coating. The corrosion problem is even more acute after welding of AZ31 parts. Mostly the filler wire used in welding is more highly alloyed so the welded seam and the bulk material act as galvanic cells. In addition, the grain structure of the alloy changes in the heat affected zone (HAZ) during the joining process. This further decreases the corrosion resistance [7–9]. For this reason a protection against corrosion is especially important for the welding seam after welding. Currently, joined complete magnesium parts can be protected by a variety of approved methods, e.g., Anomag®, Magoxid-COAT®, Keronite® [3, 10–12]. The major disadvantage of these methods is that they have to be applied in an additional process step which opens a time frame for corrosion generally in the sensitive areas of welded seams. Furthermore, some of these methods, e.g., the application of chromate layers and fluoridation procedures carried out with hydrofluoric acid, contain high risks for health, and environment.

Despite of the fact that the corrosion of magnesium alloys is a major problem in the engineering industries, this feature has enabled medical applications of these alloys as temporary implants, for example in the support of fractured bones or as vascular stents [13–20]. The controlled degradation of the implant material is of interest when in this way a second operation can be avoided (which may be necessary, for example, when bone-supporting structures made of standard implant materials like titanium are used) or when the implant-carrying person is still a growing child. In this domain, often a certain reduction of the corrosion rate of the magnesium alloy is necessary which can be achieved by coating the implant with a thin anti-corrosive layer. The use of magnesium fluoride coatings becomes more and more important here, since studies have shown that nanoparticles of this substance have an antibacterial effect in vivo [21]. Owing to the strong ionic bond and chemical resistance a protective layer composed of magnesium fluoride offers great advantages [20].

For the deposition of dense magnesium fluoride layers onto magnesium alloys the suspension plasma spraying (SPS) process appears suitable [22, 23]. SPS methods have been widely used to obtain a rich variety of deposits on almost any kind of substrate [24–29]. In contrast to conventional plasma spraying (CPS) where powder material is being fused and accelerated toward the substrate via a plasma jet, the SPS offers the opportunity to use submicrometer particles dispersed in a liquid feedstock, e.g., water or ethanol. By the use of submicrometer feedstock particles, dense and finely grained layers can be produced [23].

Nanocrystalline fluorides can be easily synthesized via a polyol-mediated approach, in which a polyalcohol (e.g., diethylene glycol, DEG) serves as both high-boiling solvent and surface-capping group [30]. In contrast to other bottom-up procedures, e.g., micelle approaches, gram scale batches are easy to perform. Although in the past decade, many nanoscale inorganic fluorides had been obtained by this method, the polyol-mediated synthesis of magnesium fluoride has not been described before [31–33]. By the addition of rare earth element salts during the synthesis, these can be doped into the product to obtain fluorescence-labeled nanoparticles [34, 35]. Such luminescent nanoparticles are promising materials for labeling under harsh conditions due to the pronounced temperature and chemical resistance of inorganic fluorides [36].

In this study, we describe the synthesis of nanocrystalline magnesium fluoride particles, the preparation of suitable suspensions with high solid loads and their application in a stepwise TIG/SPS process. The particles can be co-doped with Ce^{3+} and Tb^{3+}, yielding a bright green emission under UV light. The nanoparticles, their suspensions as well as coatings prepared by SPS are thoroughly characterized using physico-chemical methods. In addition, first investigations on the anti-corrosive properties of the resulting magnesium fluoride coatings are reported.

Experimental section

Synthesis of the suspensions

All reactions were carried out under argon and with chemicals purchased from Sigma-Aldrich. For a typical batch, 17.16 g magnesium acetate tetrahydrate (80 mmol, 99%) was dissolved under vigorous stirring in 400 mL DEG (99%) at 100 °C in a three-necked flask equipped with a Claisen still head. The temperature was further increased up to 200 °C. At this point, a solution of 5.93 g ammonium fluoride (160 mmol, ≥98%) in 300 mL DEG, kept at 100 °C, was added quickly to the metal salt solution. The combined solutions were stirred for an additional 2 h at 200 °C to increase crystallinity and then cooled to room temperature. Separation of the solid material was achieved by centrifugation at 16000 g (benchtop centrifuge Universal 320 from Hettich Lab Technology). Afterwards, the material was washed three times with ethanol by redispersion and centrifugation steps. Finally, after drying overnight a white

powder in nearly quantitative yield was obtained. From this powder, suspensions of nanocrystalline magnesium fluoride in water with up to 5 mass% can easily be formulated by a short ultrasonic treatment. Such suspensions are stable for at least several months. Fluorescence labeling was achieved by a similar procedure as described above; in addition to the magnesium acetate, 1.41 g cerium(III) acetate hydrate (4.44 mmol, 99.9%) and 1.66 g terbium(III) chloride hexahydrate (4.44 mmol, 99.9%) were supplied to the metal salt solution in DEG. The amount of ammonium fluoride was increased accordingly.

Methods of characterization

Powder X-ray diffraction (PXRD) data were recorded on a STOE StadiP diffractometer in transmission mode. X-ray diffraction (XRD) investigations on the coatings were carried out with a STOE Theta–Theta in reflection geometry. Both diffractometers were equipped with monochromatized CuKα_1 radiation. Nanocrystal sizes were estimated with the Scherrer's equation from the reflection broadening after elimination of the experimental broadening with a Si standard. Transmission electron microscope (TEM) characterization of the nanoparticles was performed on a JEOL JEM-2100F-UHR with an accelerator voltage of 200 kV. The samples were dispersed in ethanol dropped on a carbon-copper grid and the ethanol was removed by evaporation. Scanning electron microscopy (SEM) investigations on welded and coated seams on AZ31 sheets were realized with a JEOL JSM-6700F cold field-emission scanning electron microscope (FE-SEM) equipped with a semi in lens and a secondary electron detector under acceleration voltages between 2 and 7 kV. Energy dispersive X-ray (EDX) spectra were measured with an INCA 300 EDX detector from Oxford Instruments attached to the FE-SEM.

Samples for cross-section SEM micrographs were embedded into polymer, and sputtered with gold after cutting and grinding. UV–vis spectra were recorded on a Cary 5E spectrometer (Varian). Luminescence excitation and emission spectra were measured with a Fluorolog III UV–vis–NIR fluorescence spectrometer (Horiba Jobin-Yvon) on powder samples at room temperature.

The potentiodynamic polarization measurements were performed with a modified MiniCell from Ibendorf & Co. (0.8 mm^2 measuring surface) equipped with an Ag/AgCl counter electrode. Samples were measured in a 0.9% NaCl electrolyte with a scanning rate of 5 ms against an Ag/AgCl counter electrode. The results of the current density potential curves were evaluated and are based on the half logarithmic scale of the current density diagram and the Tafel extrapolation for all tests by MATLAB using the Butler Volmer equation. A limit value determination of the data points for the negative and positive potential limit as well as the OCP were carried out (by a previous minimum value determination) within the program. The determination of the dividing lines as well as the regression lines are carried out in the established limits of the linear sector of both graph branches. Using the standard deviation over the complete measuring time period the program calculates the exchange current density and the mean average value of the equilibrium rest potential. The values were converted into normal hydrogen electrode (NHE) potentials.

For dynamic light scattering experiments and zeta potential measurements a Zetasizer Nano ZS from Malvern Instruments equipped with an MPT-2 autotitrator was used. The values of pH, for pH-dependent zeta potential measurements, were adjusted with 0.1 M solutions of HCl and NaOH. A rotational viscometer Viscotester 7L/R from Haake was used to perform viscosity measurements on the magnesium fluoride suspensions at 25 °C.

Tungsten inert gas welding

The welding experiments were realized on AZ31 sheets ($h = 6$ mm) with a filler wire of AZ31X. The compositions of the AZ31 sheets and the AZ31X filler wire are listed in Table 1. On top welded seams were created with a robot assisted welder TETRIX 521 AC/DC activArc from EWM Hightec Welding in AC operating mode (welding current: 170 A; inert gas: Argon 4.6 (8 L/min); filler wire: AZ31X, diameter: 1.2 mm; wire feed: 1.4 m/min).

Suspension plasma spraying

The welded seams created on the AZ31 sheets were suspension plasma sprayed in a separate step with a Sulzer Metco Triplex II torch attached on an ABB industrial robot. The operating parameters were as follows: spray distance: 95 mm; working gas: 35 slpm Ar and 25 slpm He; arc current: 450 A; injection rate 25% (4.5 kg/h) with 2.4 bar, without atomizing gas; torch velocity: 1.5 m/s. Welded seams were coated in three passes with 5 mm parallel line-offset.

Table 1 Compositions of the AZ31 bulk material and the AZ31X filler wire in percent (residual percentages: Mg)

	Al	Zn	Mn	Si	Fe	Cu	Ni	Sn	AE	AZ
AZ31	3.29	0.95	0.24	0.02	0.029	0.013	0.004	0.016	–	–
AZ31X	2.92	1.05	0.29	0.01	0.002	0.0003	0.0004	–	<0.05	<0.3

Results

Using the procedure described in the experimental section, magnesium fluoride precipitates phase pure and in a nanocrystalline form, as can be judged from the PXRD pattern of nanocrystalline magnesium fluoride (Fig. 1). The broadened signals reflect the nanocrystalline character of the sample. Quantitative evaluation based on Scherrer's equation, applied to the (110) reflection of MgF_2, gives a size of ca. 5 nm for the coherently scattering regions. This is in a good agreement with the results of HR-TEM investigations which show slightly agglomerated particles with sizes from 2 to 7 nm (Fig. 2). The co-doping pair Ce^{3+} and Tb^{3+} is frequently used to yield bright green fluorescence under UV irradiation [34, 35, 37–40]. In this case, the Ce^{3+} ions act in general as efficient sensitizers for Tb^{3+} ions due to the parity allowed $4f^1 \leftrightarrow 5d^1$ electronic transitions. The energy transfer mechanism between the cerium and terbium ions is reported in detail elsewhere and is used for the green phosphor in discharge lamps since many years [34, 40]. In this study the optical properties of Ce^{3+} and Tb^{3+} co-doped MgF_2 nanoparticles show bright green emission under UV excitation which is investigated by UV–vis reflection and luminescence spectroscopy. As presented in Fig. 3 the room temperature excitation spectrum (b) consists of broad bands starting at 300 nm and peaking at 255 nm, which can be assigned to Ce^{3+} $4f^1 \rightarrow 5d^1$ electronic transitions. The respective emission spectrum (c) exhibits four emission peaks (470–633 nm) followed by much more diffuse signals (636–699 nm), which corresponds to Tb^{3+} relaxation starting at the excited $^5D_4$ state to the ^7F_J ($J = 6$–0) ground states. No resolution of the crystal field levels is observed which can be explained by the small size of the particles. A broad emission with lower intensity and a maximum at 332 nm can be assigned to $5d^1 \rightarrow 4f^1$ transitions of Ce^{3+} [37, 40]. The high efficiency of $Ce^{3+} \rightarrow Tb^{3+}$ energy transfer is obvious by comparing the intensities of Ce emission relative to Tb emission within the emission spectrum at Ce excitation. The UV–vis reflection spectrum exhibits Ce^{3+} transitions also observed in the excitation spectrum but with different intensities (Fig. 3a and b). This can be explained by the fact that the lowest 5d states lead to stronger emission, in spite of its lower absorption intensity. No direct excitation of the Tb^{3+} appears in both, reflection and excitation spectra due to the high efficiency of the energy transfer process and the low absorption probability of the parity forbidden transitions. The determination of a particle size distribution based on the hydrodynamic diameters as determined by DLS is shown in Fig. 4 (left). The DLS graph reveals a monomodal particle size distribution centered at about 10 nm. Taking into account that hydrodynamic diameters are in general larger than

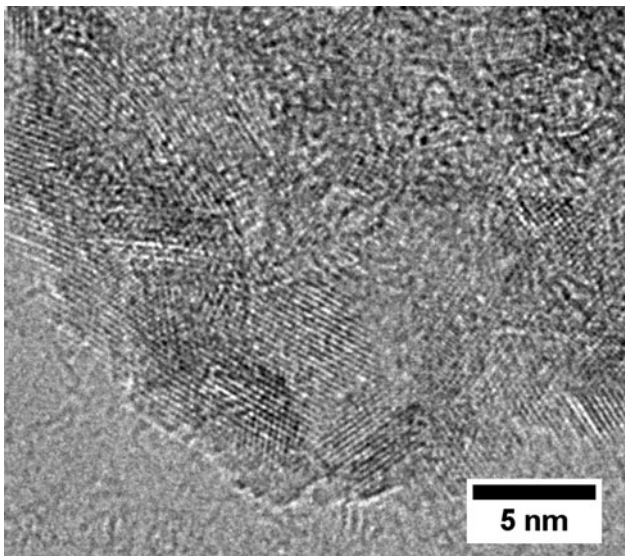

Fig. 2 High resolution transmission electron micrograph of MgF_2 nanoparticles

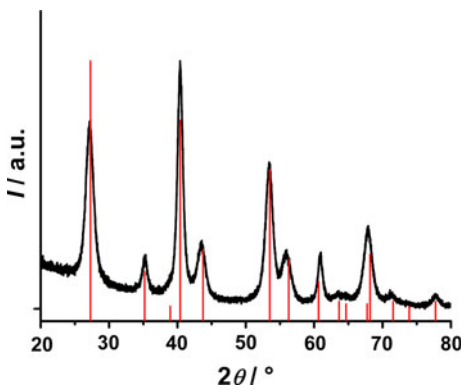

Fig. 1 Powder X-ray diffraction pattern of MgF_2 nanocrystals. Pattern of reference is given as line diagram, pdf card 41-1443 (MgF_2)

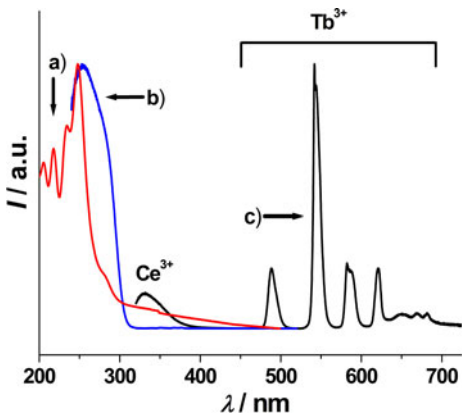

Fig. 3 Optical investigations of MgF_2:Ce^{3+}/Tb^{3+} powder samples at room temperature. (*a*) UV–vis reflection spectrum (*red*); (*b*) luminescence excitation spectrum (*blue*), $\lambda_{em} = 545$ nm; (*c*) fluorescence emission spectrum (*black*), $\lambda_{ex} = 285$ nm (Color figure online)

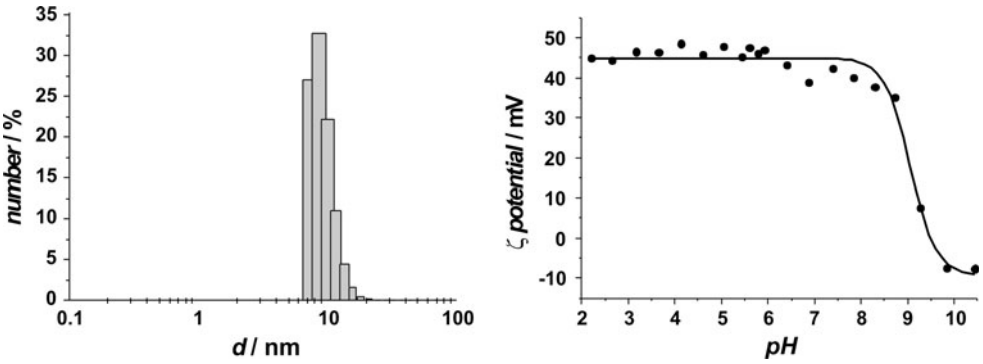

Fig. 4 *Left* distribution of the hydrodynamic diameters of MgF_2 nanoparticles in an aqueous suspension as determined by dynamic light scattering (DLS). *Right* Zeta potential of MgF_2 nanoparticles versus pH in an aqueous suspension

crystallite sizes determined by broadening of PXRD peaks or particle sizes observed in electron microscopy, this result indicates that the suspension contains individual hydrated nanoparticles, i.e., no agglomeration or aggregation occurs in the dispersion [41]. The basis for this behavior as well as the long time stability of the suspensions can be traced back to the high positive zeta potential of the particles which stabilizes them via electrostatic repulsion (Fig. 4, right).

In Fig. 5 a viscosity measurement of the magnesium fluoride suspension, which was used for the suspension plasma spraying, is plotted. The shear rate dependence of the viscosity reveals a shear-thinning (pseudoplastic) flow behavior. With increasing shear rates, the viscosity decreases due to breaking of particle–particle interactions in the suspension, permitting much easier flow [42, 43]. However, such attractions seem to have no influence on the sedimentation stability of the suspensions and the viscosity observed even at low shear rates is not an issue for the use in the SPS process.

Figure 6a shows a sheet of the AZ31-base material. Welded traces of the filler wire material were prepared on such AZ31 sheets by TIG welding. Such a trace, 6 mm thick and 80 mm wide, resembling a true welding seam, is shown in Fig. 6b. For the SPS process, a 5 mass% suspension of nanocrystalline magnesium fluoride in water was prepared by short ultrasonification. This suspension was plasma-sprayed on the welded seam with the parameter described above. The product of this procedure is shown in Fig. 6c. An SEM cross-section and EDX analyses of the coated seams are shown in Fig. 7. The SEM micrograph displays that the magnesium fluoride layer on top of the welded seam is about 10 μm thick. The layer is continuous and dense with fine grain sizes. The EDX mapping reveals a clear borderline between the welded seam and the coating, with no fluorine being detectable in the welded seam. Correspondingly, the coating procedure did not affect the seam and the bulk AZ31 material. When a suspension containing co-doped nanoparticles is used (MgF_2:Ce^{3+}/Tb^{3+} with 5 wt% in water), the presence of the generated coating can easily be monitored due to the strong green fluorescence it emits under UV light (Fig. 8). This shows that the fluorescent labeling persists also after the harsh conditions of SPS.

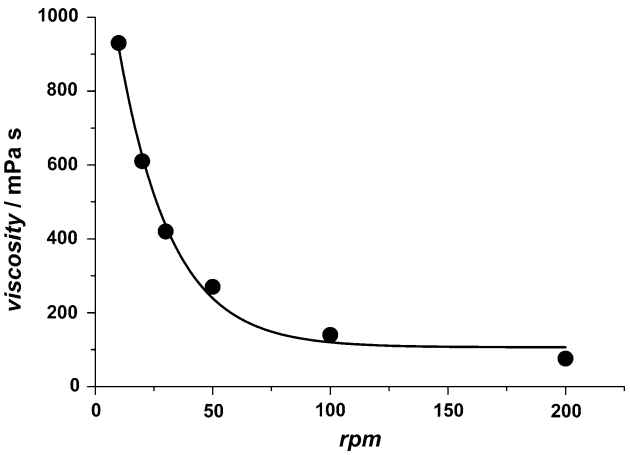

Fig. 5 Viscosity of a magnesium fluoride (5 wt%) suspension in water

The magnesium fluoride coating was further characterized by HR-SEM and XRD studies. The HR-SEM micrograph in Fig. 9 shows in addition to some larger accretions a very finely grained surface. This indicates that the magnesium fluoride nanoparticles supplied via the suspension probably reach the surface of the welded seam in their original state, i.e., with negligible aggregation and without melting. In fact, the parameters of the suspension plasma spraying were chosen to induce as little as possible heat on the suspension droplets to avoid melting or evaporation of the sub 10 nm particles. XRD experiments of the covered welded seam show both, sharp reflections for the AZ31 bulk material and broad reflections corresponding to the nanocrystalline magnesium fluoride layer (Fig. 10). Calculating the particle size from the reflection broadening of the diffractogram of magnesium fluoride gives a particle diameter of ca. 7 nm, i.e., the particle size has not increased during the SPS process. This confirms that the originally suspended particles reached the surface as

Fig. 6 Photographic images: **a** AZ31 raw material sheet; **b** a TIG welded seam of AZ31X on an AZ31 sheet; **c** coating of the welded seam prepared by SPS. The sample shown in **c** was cut in order to prepare the cross-section image shown in Fig. 7

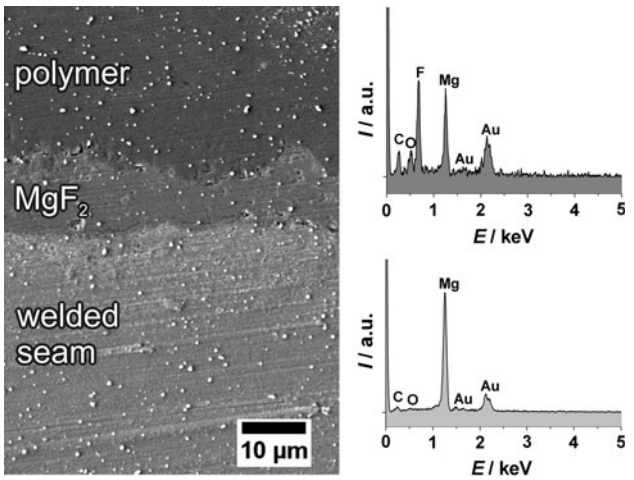

Fig. 7 *Left* SEM cross-section micrograph of a welded seam coated with a magnesium fluoride layer. On top of the image the polymer in which the sample was embedded is visible. Small bright spots littering the cross-section are due to gold sputtering of the sample. *Right* EDX spectra of selected areas (*bottom* raw AZ31 material; *top* magnesium fluoride layer)

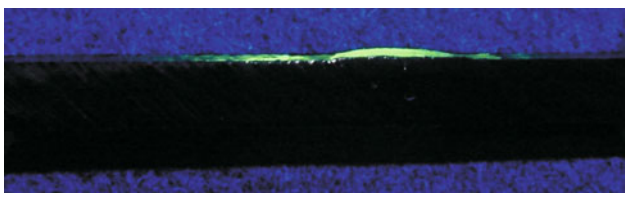

Fig. 8 Cross-section photography of the coating on a welded seam on AZ31. The AZ31 sheet which appears *black* in the photography has a thickness of 6 mm. The coating was produced using a suspension of doped magnesium fluoride nanoparticles (MgF_2:Ce^{3+}/Tb^{3+}). The presence of the film is confirmed by the *bright green area* appearing under irradiation with UV light (254 nm) (Color figure online)

nanoparticles. The absence of any signals from oxide/hydroxide phases in the XRD pattern displays that neither hydrolysis nor an exchange of fluoride against oxide ions has occurred. Oxide/hydroxide formation could in principle have been caused by incomplete evaporation of the suspension water.

For a first evaluation of the corrosion-protective properties of the magnesium fluoride coating, a comparative

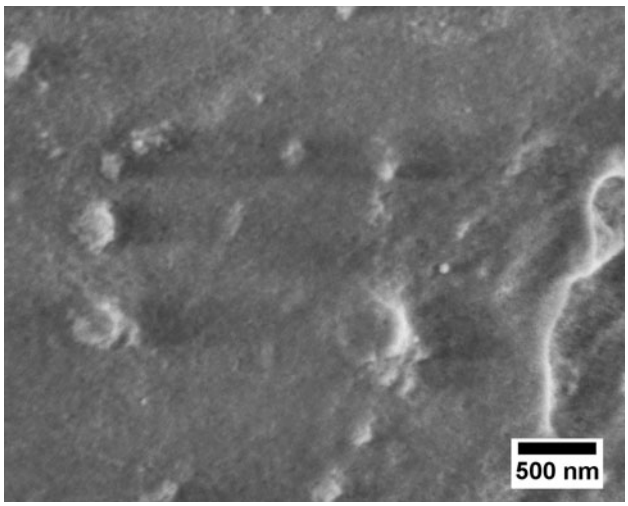

Fig. 9 High resolution scanning electron micrograph of a magnesium fluoride coating produced by SPS on a welded seam

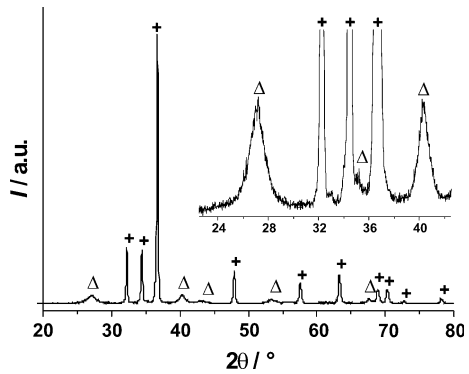

Fig. 10 XRD pattern of a magnesium fluoride coating produced by SPS on a welded seam. *Inset* 20-fold magnification of a selected 2θ range. The signals can be assigned to MgF_2 and Mg: (*open triangle*) pdf card 41-1443 (MgF_2) (+) pdf card 35-821 (magnesium)

potentiodynamic polarization measurement was carried out (Figure 11). The values of i_{corr}, which are directly proportional to the corrosion rate P_i ($P_i = 22.85 * i_{corr}$), can be used to compare the corrosion properties between our specimens [44, 45]. However, P_i values have to be interpreted cautiously. Owing to the negative difference effect (NDE), corrosion rates for magnesium and magnesium

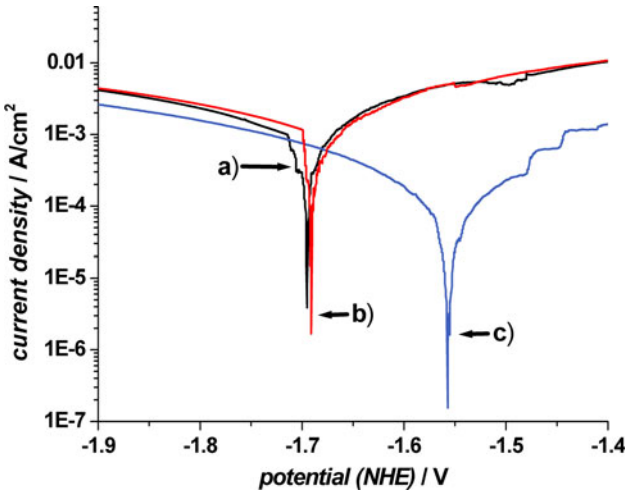

Fig. 11 Potentiodynamic polarization curves of (*a*) the AZ31 raw material (*black*), (*b*) the TIG-welded seam on an AZ31 sheet (*red*) and (*c*) the TIG-welded seam equipped with a magnesium fluoride coating (*blue*) (Color figure online)

Table 2 Results of the potentiodynamic polarization measurements for the AZ31 blank material, the TIG-welded seam on the AZ31 material, and for the magnesium fluoride-coated seam

	E_{corr}/V vs. NHE	i_{corr}/A cm^{-2}	P_i/mm y^{-1}
Blank AZ31	−1.70	5.0×10^{-5}	1.14×10^{-3}
Welded seam	−1.69	9.1×10^{-5}	2.08×10^{-3}
MgF_2-coated seam	−1.56	0.4×10^{-5}	9.14×10^{-5}

NHE normal hydrogen electrode. The values of the corresponding corrosion rates were calculated using $P_i = 22.85 i_{corr}$

alloys determined via Tafel extrapolation typically underestimate the real corrosion rate [5, 6, 45, 46]. However, here the aim was to compare the corrosion properties of a blank sample of AZ31, of an uncoated welded seam produced by TIG, and of a welded seam covered with a magnesium fluoride coating layer prepared by SPS. The values for E_{corr}, i_{corr}, and P_i are listed and compared in Table 2.

The blank AZ31 sheet and the TIG-welded AZ31 material show very similar values for E_{corr}, shifting only slightly between −1.70 and −1.69 V. After TIG welding, the current density i_{corr} for the welded AZ31 sheet is nearly twice as large as the value of i_{corr} for the blank AZ31. This could be caused by a different alloy composition of the welded seam compared with the blank material (see Table 1) and/or the material disorder which in general makes welded seams more susceptible for corrosion. For the magnesium fluoride-coated seam, a strong shift of E_{corr} to a more positive value of −1.56 V is observed. The current density i_{corr} of the magnesium fluoride-coated seam is ca. 23-fold smaller than i_{corr} of the uncoated welded seam. From this finding it can be judged that the corrosion rate of welded seams between magnesium components can be reduced significantly by the process presented here, which consists in the application of a magnesium fluoride layer by using a suspension of MgF_2 nanoparticles in a suspension plasma spraying process.

Conclusions

This study demonstrates the possibility to deposit an anti-corrosive layer, based on nanocrystalline MgF_2 and applied via a suspension plasma spraying process on welding seams of a magnesium alloy. The study encompasses the chemical synthesis of the nanoparticles, the preparation of suitable suspensions and the coating of the welding seams, including thorough characterization of the materials and the coating as well as a preliminary corrosion test. Based on our experimental results following conclusions can be made:

- Nanocrystalline MgF_2 particles can easily be synthesized by a polyol-mediated approach.
- Stable aqueous MgF_2 suspensions with solid loads of 5 mass% can be formulated without the use of surfactants.
- By the use of those MgF_2 suspensions in a suspension plasma spraying process, dense layers of nanocrystalline MgF_2 can be applied on AZ31 alloy sheets.
- Welded seams on AZ31 coated with such a MgF_2 layer by SPS show a significant lower corrosion rate.
- When luminescent MgF_2 nanoparticles were used, film quality can easily be monitored by UV light.

We consider that a simultaneous process, where the SPS process is applied directly after the TIG welding, should be possible. On the one hand, this TIG-SPS combination would enhance the productivity enormously. On the other hand, when the magnesium fluoride coating is prepared directly on the still hot welded seam, this would drastically minimize the exposure of the fresh and sensitive welded seam to corrosive environments and could also lead to even denser layers. Thus, our aim is to develop a hybrid TIG-SPS process in which a TIG welder is attached in front of a SPS torch to weld and protect magnesium joints in one step.

Acknowledgements We gratefully acknowledge the financial support of the Volkswagen foundation via the research initiative "Innovative Methods for Manufacturing Multifunctional Surfaces".

References

1. Makar GL, Kruger J (1993) Int Mater Rev 38:3
2. Song G (2005) Adv Eng Mater 7(7):563

3. Gray JE, Luan B (2002) J Alloys Compd 336:88
4. Ghali E, Dietzel W, Kainer K-U (2004) J Mater Eng Perform 13:7
5. Song G, Atrens A (2003) Adv Eng Mater doi:10.1002/adem.200310405
6. Song G, Atrens A (1999) Adv Eng Mater 1:11
7. Thate W, Zschetzsche J (2003) wt Werkstattstechnik online 10:699
8. Xu RZ, Song G, Wang Z (2009) Mater Res Innov 13:441
9. Zeng R-C, Chen J, Dietzel W, Zettler R, dos Santos JF, Nascimento ML, Kainer KU (2009) Corros Sci 51:1738
10. Kurze P (1998) Mat-wiss Werkstofftech 29:85
11. Yerokhin AL, Shatrov A, Samsonov V, Shashkov P, Leyland A, Matthews A (2004) Surf Coat Technol. doi:10.1016/S0257-8972(03)00877-6
12. Blawert C, Hort N, Kainer KU (2004) Trans Indian Inst Met 57:397
13. Witte F, Fischer J, Nellesen J, Vogt C, Vogt J, Donath T, Beckmann F (2009) Acta Biomater. doi:10.1016/j.actbio.2009.10.012
14. Alvarez-Lopez M, Pereda MD, del Valle JA, Fernandez-Lorenzo M, Garcia-Alonso MC, Ruano OA, Escudero ML (2009) Acta Biomater. doi:10.1016/j.actbio.2009.04.041
15. Chiu KY, Wong MH, Cheng FT, Man HC (2007) Surf Coat Technol 202:590
16. Brar HS, Platt MO, Sarntinoranont M, Martin PI, Manuel M (2009) J Miner Met Mater Soc. doi:10.1007/s11837-009-0129-0
17. Krause A, von der Höh D, Bormann D, Krause C, Bach F-W, Windhagen H, Meyer-Lindenberg A (2010) J Mater Sci. doi:10.1007/s10853-009-3936-3
18. Li JN, Cao P, Zhang XN, Zhang SX, He YH (2010) J Mater Sci. doi:10.1007/s10853-010-4688-9
19. Li Y, Hodgson PD, Wen C (2011) J Mater Sci. doi:10.1007/s10853-010-4843-3
20. Bach Fr-W, Hassel T, Krause C, Wilk P (2005) In: Neelamaghan NR, Kaplan HI, Powell BR (eds) Magnesium technology 2005. TMS, Warrendale
21. Lellouche J, Kahana E, Elias S, Gedanken A, Banin E (2009) Biomater 30:5969
22. Toma F-L, Berger L-M, Naumann T, Langer S (2008) Surf Coat Technol 202:4343
23. Pawlowski L (2009) Surf Coat Technol 203:2807
24. Kozerski S, Pawlowski L, Jaworski R, Roudet F, Petit F (2009) Surf Coat Technol. doi:10.1016/j.surfcoat.2009.09.020
25. Chen Z, Trice RW, Besser M, Yang X, Sordelet D (2004) J Mater Sci 39:4171
26. Burlacov I, Jirkovsky J, Müller M, Heinmann RB (2006) Surf Coat Technol 201:255
27. Tomaszek R, Pawlowski L, Gengembre L, Laureyns J, Znamirowski Z, Zdanowski J (2006) Surf Coat Technol 201:45
28. Wittmann-Teneze K, Valle K, Bianchi L, Belleville P, Caron N (2008) Surf Coat Technol 202:4349
29. Jaworski R, Pawlowski L, Pierlot C (2009) Thermal Spray. doi:10.1361/cp2009itsc0156
30. Feldmann C (2005) Solid State Sci 7:868
31. Feldmann C, Roming M, Trampert K (2006) Small 2:1248
32. Eiden-Assmann S, Maret G (2004) Mater Res Bull 39:21
33. Wei Y, Lu F, Zhang X, Chen D (2007) Mater Lett 61:1337
34. Wang ZL, Quan ZW, Jia PY, Lin CK, Luo Y, Chen Y, Fang J, Zhou W, O'Connor CJ, Lin J (2006) Chem Mater. doi:10.1021/cm052360x
35. Kong D, Wang ZL, Lin CK, Quan ZW, Li YY, Li CX, Lin J (2007) Nanotechnology. doi:10.1088/0957-4484/18/7/075601
36. Kuznetsov S, Osiko V, Tkatchenko E, Fedorov P (2006) Russ Chem Rev 75:1065
37. Riwotzki K, Meyssamy H, Schnablegger H, Kornowski A, Haase M (2001) Angew Chem Int Ed 113:574
38. Heinroth F, Gruss D, Müller S, Waltz F, Martynczuk J, Feldhoff A, Behrens P, Wiebcke M (2009) J Mater Sci. doi:10.1007/s10853-009-4130-3
39. Heinroth F, Waltz F, Wiebcke M, Behrens P (2008) Z Anorg Allg Chem. doi:10.1002/zaac.200870073
40. Sokolnicki J (2010) J Phys : Condens Mater doi:10.1088/0953-8984/22/27/275301
41. Zanetti-Ramos BG, Fritzen-Garcia MB, Creczynski-Pasa TB, De Oliveira CS, Pasa AA, Soldi V, Borsali R (2010) Part Sci Technol. doi:10.1080/02726351.2010.504133
42. Tseng WJ, Lin K-C (2002) Mater Sci Eng A. doi:10.1016/S0921-5093(03)00063-7
43. Kong D, Yang H, Yang Y, Wei S, Wang J, Cheng B (2004) Mater Lett. doi:10.1016/j.matlet.2004.06.060
44. Witte F, Fischer J, Nellesen J, Crostack H-A, Kaese V, Pisch A, Beckmann F, Windhagen H (2006) Biomaterials. doi:10.1016/j.biomaterials.2005.07.037
45. Shi Z, Liu M, Atrens A (2009) Corros Sci. doi:10.1016/j.corsci.2009.10.016
46. Song G, Atrens A, Dargusch M (1999) Corros Sci. doi:10.1016/S00-10-938X(98)00121-8